
Structure-preserving Gaussian Process Dynamics

Katharina Ensinger^{1,2} Friedrich Solowjow² Sebastian Ziesche¹
Michael Tiemann¹ Sebastian Trimpe²

¹Bosch Center for Artificial Intelligence, Renningen, Germany

²Institute for Data Science in Mechanical Engineering, RWTH Aachen University, Aachen, Germany

Abstract

Most physical processes possess structural properties such as constant energies, volumes, and other invariants over time. When learning models of such dynamical systems, it is critical to respect these invariants to ensure accurate predictions and physically meaningful behavior. Strikingly, state-of-the-art methods in Gaussian process (GP) dynamics model learning are not addressing this issue. On the other hand, classical numerical integrators are specifically designed to preserve these crucial properties through time. We propose to combine the advantages of GPs as function approximators with structure preserving numerical integrators for dynamical systems, such as Runge-Kutta methods. These integrators assume access to the ground truth dynamics and require evaluations of intermediate and future time steps that are unknown in a learning-based scenario. This makes direct inference of the GP dynamics, with embedded numerical scheme, intractable. Our key technical contribution is the evaluation of the implicitly defined Runge-Kutta transition probability. In a nutshell, we introduce an implicit layer for GP regression, which is embedded into a variational inference-based model learning scheme.

1 Introduction

Many physical processes can be described by an autonomous continuous-time dynamical system

$$\dot{x}(t) = f(x(t)) \text{ with } f : \mathbb{R}^d \rightarrow \mathbb{R}^d. \quad (1)$$

Dynamics model learning deals with the problem of estimating the function f from sampled data. In prac-

tice, it is not possible to observe state trajectories in continuous time since data is typically collected on digital sensors and hardware. Thus, we obtain noisy discrete-time observations

$$\{\hat{x}_n\}_{1:N} = \{x_1 + \nu_1, \dots, x_N + \nu_N\}, \quad (2)$$
$$\nu_n \sim \mathcal{N}(0, \text{diag}(\sigma_{n,1}^2, \dots, \sigma_{n,d}^2)).$$

Accordingly, models of dynamical systems are typically learned as one-step ahead-predictions

$$x_{n+1} = g(x_n). \quad (3)$$

Especially, Gaussian processes (GPs) have been popular for model learning and are predominantly applied to one step ahead predictions (3) [6, 10, 7, 4]. However, there is a discrepancy between the continuous (1) and discrete-time (3) systems. Importantly, (1) often possesses invariants that represent physical properties. Thus, naively chosen discretizations might lead to poor models.

Numerical integrators provide sophisticated tools to efficiently discretize continuous-time dynamics (1). Strikingly, one step ahead predictions (3) correspond to the explicit Euler integrator $x_{n+1} = x_n + hf(x_n)$ with step size h . This follows immediately by identifying $g(x_n)$ with $x_n + hf(x_n)$. It is well-known that the explicit Euler method might lead to problematic behavior and suboptimal performance [17]. Clearly, this raises the immediate question: *can superior numerical integrators be leveraged for dynamics model learning?* For the numerical integration of dynamical systems, the function f is assumed to be known. The explicit Euler is a popular and straightforward method, which thrives on its simplicity. No intermediate evaluations of the dynamics are necessary, which makes the integrator also attractive for model learning. While this behavior is tempting when implementing the algorithm, there are theoretical issues [17]. In particular, important physical and geometrical structure is not preserved. In contrast to the explicit Euler, there are also implicit and higher-order methods. However, these generalizations require the evaluation at intermediate and future time steps,

which leads to a nonlinear system of equations that needs to be solved. While these schemes become more involved, they yield advantageous theoretical guarantees. In particular, Runge-Kutta (RK) schemes define a rich class of powerful integrators. Despite assuming the dynamics function f to be unknown, we can still benefit from the discretization properties of numerical integrators for model learning. To this end, we propose to combine GP dynamics learning with arbitrary RK integrators, in particular, implicit RK integrators.

Depending on the problem that is addressed, the specific RK method has to be tailored to the system. As an example, we consider structure-preserving integrators, i.e., geometric and symplectic ones. We develop our arguments based on Hamiltonian systems [36, 35, 12]. These are an important class of problems that preserve a generalized notion of energy and volume. Symplectic integrators are designed to cope with this type of problems providing volume-preserving trajectories and accurate approximation of the total energy [16]. In order to demonstrate the flexibility of our method, we also introduce a geometric integrator that is consistent with a mass moving on a surface. For both examples, we show in the experiments section that the predictions with our tailored GP model are indeed preserving the desired structure.

By generalizing to more sophisticated integrators, we have to address the issue of propagating implicitly defined distributions through the dynamics. This is due to the fact that evaluations of the GP at the next time step induce additional implicit evaluations of the dynamics. Depending on the integrator, these might be future or intermediate time steps that are also unknown. On a technical level, sparse GPs provide the necessary flexibility. A decoupled sampling approach allows consistent sampling of functions from the GP posterior [44]. In contrast to previous GP dynamics modeling schemes this yields consistency throughout the entire simulation pipeline [24]. By leveraging these ideas, we derive a recurrent variational inference (VI) model learning scheme.

By addressing integrator-induced implicit transition probabilities, we are essentially proposing implicit layers for probabilistic models. Implicit layers in neural networks (NNs) are becoming increasingly popular [13, 2, 28]. However, the idea of implicitly defined layers has (to the best of our knowledge) not yet been generalized to probabilistic models like GPs.

In summary, the main contributions of this paper are:

- a general and flexible probabilistic learning framework that combines arbitrary RK integrators with GP dynamics model learning;
- deriving an inference scheme that is able to cope

with implicitly defined distributions, thus extending the idea of implicit layers from NNs to probabilistic GP models; and

- embedding geometrical and symplectic integrators, yielding structure-preserving GP models.

2 Related work

Dynamics model learning is a very broad field and has been addressed by various communities for decades, e.g., [29, 37, 27, 11]. Learning dynamics models can be addressed with a continuous time model [20, 43]. Nonparametric models were learned by applying sparse GPs [21, 19]. A common approach for learning discrete time models are Gaussian process state-space models [41, 42, 38]. In this work we consider fully observable models in contrast to common state-space models. However, we apply the tools of state-space model literature. We develop our ideas exemplary for the inference scheme proposed in Doerr et al. [7]. At the same time, our contribution is not restricted to that choice of inference scheme and can be combined with other schemes as well. Ialongo et al. [24] have criticized the inference scheme and shown that there might be issues in the presence of transition noise and the inference might become inconsistent. However, none of these concerns are relevant to our work since we omit transition noise and sample GPs from the posterior (cf. Sec. 4.)

Implicit transitions have become popular for NNs and provide useful tools and ideas that we leverage. In general, implicit transitions are cast into an optimization problem [13]. On a technical level, we implement related techniques based on the implicit function theorem and backpropagation. In Pan et al. [30], implicit transition functions are used to perform multi-modal regression tasks. A NN with infinitely many layers was trained by implicitly defining the equilibrium of the network [2]. Look et al. [28] proposed an efficient backpropagation scheme for implicitly defined neural network layers. All these approaches refer to deterministic NNs, while we extend the ideas to probabilistic GP models.

Including Hamiltonian structure into learning in order to preserve physical properties of the system, is an important problem addressed by many sides. The problem can be tackled by approximating the continuous time Hamiltonian structure from data. This was addressed by applying a NN [14]. Since modern NN approaches provide a challenging benchmark, we compare our method against Greydanus et al. [14]. In Jin et al. [25], the Hamiltonian structure is learned by stacking multiple symplectic modules. Gaussian processes have been combined with symplectic structure [33]. In contrast to our approach, the focus lies

on learning continuous-time dynamics for Hamiltonian systems and unrolling the dynamics via certain symplectic integrators. In Brüdigam et al. [3] variational integrators are applied to a continuous-time GP dynamics model. In contrast to our approach the integrator step is decoupled from the learning step.

However, there is literature that addresses discrete time Hamiltonian systems. The Hamiltonian neural network approach was extended by a recurrent NN coupled with a symplectic integrator [5]. In Saemundsson et al. [34], the symplectic approach was combined with uncertainty information by applying variational autoencoders. Zhong et al. [46] extends previous approaches by adding control input. The stable nature of explicit symplectic integrators is leveraged to build the architecture of a NN by introducing symplectic transitions between the layers of a NN [15]. In contrast to previous approaches, we are able to address non-separable Hamiltonians via implicit integrators.

3 Technical background and main idea

Next, we make our problem mathematically precise and provide a summary of the preliminaries.

3.1 Gaussian process regression

A GP is a distribution over functions [32]. Similar to a normal distribution, a GP is determined by its mean function $m(x)$ and covariance function $k(x, y)$. We assume the prior mean to be zero.

Standard GP inference: For direct training, the GP predictive distribution is obtained by conditioning on n observed data points. In addition to optimizing the hyperparameters, a system of equations has to be solved, which has a complexity of $\mathcal{O}(n^3)$. Clearly, this is problematic for large datasets.

Variational sparse GP: The GP can be sparsified by introducing pseudo inputs [40]. Intuitively, we approximate the posterior with a lower number of training points. However, this makes direct inference intractable. An elegant approximation strategy is based on casting Bayesian inference as an optimization problem. We consider pseudo inputs $\xi = [\xi_1, \dots, \xi_P]$ and targets $z = [z_1, \dots, z_P]$ as proposed in [22] and applied in [7, 24, 9]. Intuitively, the targets can be interpreted as GP observations at ξ . The posterior of pseudo targets is approximated via a variational approximation $q(z) = \mathcal{N}(\mu, \Sigma)$, where μ and Σ are adapted during training. The GP posterior distribution at inputs x^* is conditioned on the pseudo inputs resulting in a normal

distribution $f(x^*|z, \xi) \sim \mathcal{N}(\mu(x^*), \Sigma(x^*))$ with

$$\begin{aligned} \mu(x^*) &= k(x^*, \xi)k(\xi, \xi)^{-1}z \\ \Sigma(x^*) &= k(x^*, x^*) - k(x^*, \xi)k(\xi, \xi)^{-1}k(\xi, x^*). \end{aligned} \quad (4)$$

Decoupled sampling: In contrast to standard (sparse) GP conditioning this allows to sample globally consistent functions from the posterior. Thus, successively sampling at multiple inputs is achieved without conditioning. By applying Matheron’s rule [23], the GP posterior is decomposed into two parts [44],

$$\begin{aligned} f(x^*|z, \xi) &= \underbrace{f(x^*)}_{\text{prior}} + \underbrace{k(x^*, \xi)k(\xi, \xi)^{-1}(z - f_z)}_{\text{update}} \\ &\approx \sum_{i=1}^S w_i \phi_i(x^*) + \sum_{j=1}^M v_j k(x^*, \xi_j)(z - f_z), \end{aligned} \quad (5)$$

where S Fourier bases ϕ_i and $w_i \sim \mathcal{N}(0, 1)$ represent the stationary GP prior [31]. For the update it holds that $v = k(\xi, \xi)^{-1}(z - \Phi W)$, $\Phi = \phi(\xi) \in \mathbb{R}^{S \times D}$. The targets z are sampled from the variational distribution $q(z)$. We add technical details in the supplementary material.

3.2 Runge-Kutta integrators

A RK integrator ψ_f for a continuous-time dynamical system f (1) is designed to approximate the solution $x(t_n)$ at discrete time steps t_n via \bar{x}_n . Hence,

$$\begin{aligned} \bar{x}_{n+1} &= \psi_f(\bar{x}_n) = \bar{x}_n + h \sum_{j=1}^s b_j g_j, \\ g_j &= f(\bar{x}_n + h \sum_{l=1}^s a_{jl} g_l), j = 1, \dots, s, \end{aligned} \quad (6)$$

where g_j are the internal stages and $\bar{x}_0 = x(0)$. We use the notation \bar{x} to indicate numerical error corrupted states and highlight the subtle difference to ground truth data. The parameters $a_{jl}, b_j \in \mathbb{R}$ determine the properties of the method, e.g., the stability radius of the method [18], the geometrical properties, or whether it is symplectic [16].

Implicit integrators: If $a_{jl} > 0$ for $l \geq j$, Eq. (6) takes evaluations at time steps into account where the state is not yet known. Therefore, the solution of a nonlinear system of equations is required. A prominent example is the implicit Euler scheme $\bar{x}_{n+1} = \bar{x}_n + hf(\bar{x}_{n+1})$.

3.3 Main idea

We propose to embed RK methods (6) into GP regression. Since the underlying ground truth dynamics

f (1) are given in continuous time, the discretization matters. Naive methods, such as the explicit Euler method, are known to be inconsistent with physical behavior. Therefore, we investigate how to learn more sophisticated models that, by design, are able to preserve physical structure of the original system. Further, we will develop this idea into a tractable inference scheme. In a nutshell, we learn GP dynamics \hat{f} that yield predictions $x_{n+1} = \psi_{\hat{f}}(x_n)$. This enforces the RK (6) instead of explicit Euler (3) structure. Thus, leading to properties like volume preservation. The main technical difficulty lies in making the implicitly defined transition probability $p(\psi_{\hat{f}}(x_n)|x_n)$ tractable.

4 Embedding Runge-Kutta integrators in GP models

Next, we dive into the technical details of merging GPs with RK integrators. We demonstrate how to evaluate the implicitly defined transition probability of any higher-order RK method by applying decoupled sampling (5). This technique is then applied to a recurrent variational inference scheme in order to obtain a GP dynamics model.

4.1 Efficient evaluation of the transition model

At its core, we consider the problem of evaluating implicitly defined distributions of RK integrators $\psi_{\hat{f}}$. To this end, we derive a sampling-based technique by leveraging decoupled sampling (5). This enables us to perform the integration step on a sample of the GP dynamics \hat{f} . The procedure is illustrated in Figure 1. We model the dynamics \hat{f} via d variational sparse GPs. Let $z \in \mathbb{R}^{d \times P}$ be a sample from the variational posterior $q(z)$ (cf. Sec. 3.1). The probability of an integrator step $p(\psi_{\hat{f}}(x_n)|z, x_n)$ is formally obtained by integrating over all possible GP dynamics $\hat{f}|z$,

$$\begin{aligned} p(x_{n+1}|z, x_n) &= p(\psi_{\hat{f}}(x_n)|z, x_n) \\ &= \int_{\hat{f}} p(\psi(x_n)|\hat{f})p(\hat{f}|z)d\hat{f}. \end{aligned} \quad (7)$$

Performing an RK integrator step $\psi_{\hat{f}}(x_n)$ requires the computation of RK stages $g^* = (g_1^*, \dots, g_s^*)$ (6)

$$g^* = \arg \min_g \|g - \hat{f}(x_n + hAg)\|^2, \quad (8)$$

with $A = (a_{jl})_{j=1, \dots, s, l=1, \dots, j}$ determined by the RK scheme (6). In the explicit case A is a sub-diagonal matrix so g_j can be calculated successively. In the implicit case, a minimization problem has to be solved. In order to sample an integrator step from (7), we first compute a GP dynamics function $\hat{f}|z$ via (5). This is

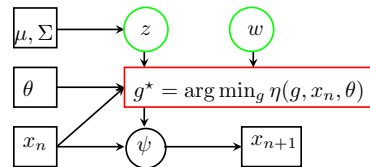


Figure 1: The evaluation of an integrator step. First, weights w and inducing targets z are sampled. This yields tractable solutions to the minimization problem for the RK stages g^* (red).

achieved by sampling inducing targets z from $\mathcal{N}(\mu, \Sigma)$ and $w \sim \mathcal{N}(0, 1)$ (cf. Sec 3.1). We are now able to evaluate \hat{f} at arbitrary locations and perform an RK integrator step with respect to the dynamics \hat{f} . To this end, the system of equations (8) is defined and solved with respect to the fixed GP dynamics \hat{f} . This enables us to extend implicit layers to probabilistic models. Combining (8) and (5) with $u = u(g) = x_n + hAg$ and $\hat{z} = z - f_z$ yields

$$g^* = \arg \min_g \left\| g - \sum_{i=1}^S w_i \phi_i(u) - \sum_{j=1}^M v_j k(u, \xi_j) \hat{z} \right\|^2. \quad (9)$$

Next, we give an example. Consider the IA-Radau method [18] $x_{n+1} = x_n + h \left(\frac{1}{4}g_1 + \frac{3}{4}g_2 \right)$, with

$$\begin{aligned} g_1 &= \hat{f} \left(x_n + \frac{h}{4}(g_1 - g_2) \right), \\ g_2 &= \hat{f} \left(x_n + h \left(\frac{1}{4}g_1 + \frac{5}{12}g_2 \right) \right). \end{aligned} \quad (10)$$

After sampling z and w , the RK scheme (10) is transformed into a minimization problem (9). With $u_1 = x_n + \frac{h}{4}(g_1 - g_2)$, $u_2 = x_n + h \left(\frac{1}{4}g_1 + \frac{5}{12}g_2 \right)$, and $\hat{z} = z - f_z$ it holds that $\left(g_1^* \right) = \arg \min_g F(g)$, with

$$F(g) = \left\| \begin{array}{l} g_1 - \sum_{i=1}^S w_i \phi_i(u_1) - \sum_{j=1}^M v_j k(u_1, \xi_j) \hat{z} \\ g_2 - \sum_{i=1}^S w_i \phi_i(u_2) - \sum_{j=1}^M v_j k(u_2, \xi_j) \hat{z} \end{array} \right\|^2. \quad (11)$$

4.2 Application to model learning via variational inference

Next, we construct a variational-inference based model learning scheme that is based on the previously introduced numerical integrators. Here, we exemplarily develop the integrators for an inference scheme similar to Doerr et al. [7] and make the method precise. It is also possible to extend the arguments to other inference schemes such as Ialongo et al. [24], Eleftheriadis et al. [8]. In contrast to Doerr et al. [7] we sample functions \hat{f} instead of independent draws from the GP

dynamics. Thus, the produced trajectory samples refer to a probabilistic, but fixed vector field. Unlike typical state-space models as Doerr et al. [7], Ialongo et al. [24] we omit transition noise. Thus, the proposed variational posterior is suitable [24]. Structure preservation is in general not possible when adding transition noise to each time step [1, §5].

Factorizing the joint distribution of noisy observations, noise-free states, inducing targets and GP posterior yields

$$p(\hat{x}_{1:N}, x_{1:N}, z, \hat{f}) = \prod_{n=0}^{N-1} p(\hat{x}_{n+1}|x_{n+1})p(x_{n+1}|x_n, \hat{f})p(\hat{f}|z)p(z). \quad (12)$$

The posterior distribution $p(x_n, z, \hat{f}|\hat{x}_n)$ is factorized and approximated by a variational distribution $q(x_n, z, \hat{f})$. Here, the variational distribution q is chosen as

$$q(x_{1:N}, z, \hat{f}) = \prod_{n=0}^{N-1} p(x_{n+1}|x_n, \hat{f})p(\hat{f}|z)q(z), \quad (13)$$

with the variational distribution $q(z)$ of the inducing targets from Section 3.1. The model is adapted by maximizing the Evidence Lower Bound (ELBO)

$$\begin{aligned} \log p(\hat{x}_{1:N}) &\geq \mathbb{E}_{q(x_{1:N}, z, \hat{f})} \left[\log \frac{p(\hat{x}_{1:N}, x_{1:N}, z, \hat{f})}{q(x_{1:N}, z, \hat{f})} \right] \\ &= \sum_{n=1}^N \mathbb{E}_{q(x_{1:N}, z, \hat{f})} [\log p(\hat{x}_n|x_n)] - \text{KL}(p(z)||q(z)) =: \mathcal{L}. \end{aligned} \quad (14)$$

Now, the model can be trained by maximizing the ELBO \mathcal{L} (14) with a sampling-based stochastic gradient descent method that optimizes the sparse inputs and hyperparameters. The expectation $\mathbb{E}_{q(x_{1:N}, z, \hat{f})} \left[\log \frac{p(\hat{x}_{1:N}, x_{1:N}, z, \hat{f})}{q(x_{1:N}, z, \hat{f})} \right]$ is approximated by drawing samples from the variational distribution $q(\hat{x}_{1:N}, z, \hat{f})$ and evaluating $p(\hat{x}_n|x_n)$ at these samples. Samples from q are drawn by first sampling pseudo targets z and a dynamics function \hat{f} from the GP posterior (5). Trajectories are produced by successively computing consistent integrator steps $x_{n+1} = \psi_{\hat{f}}(x_n)$ as described in Sec. 4.1. This yields a recurrent learning scheme, by iterating over multiple integration steps depicted in Figure 1. We are able to use our model for predictions by sampling functions from the trained posterior.

4.3 Gradients

The ELBO (14) is minimized by applying stochastic gradient descent to the hyperparameters. When conditioning on the sparse GP (4), the hyperparameters

include $\theta = (\mu_{1:d}, \Sigma_{1:d}, \theta_{1:d}^{GP})$ with variational sparse GP parameters $\mu_{1:d}$, $\Sigma_{1:d}$ and GP hyperparameters $\theta_{1:d}^{GP}$. The gradient $\frac{dx_{n+1}}{d\theta}$ depends on $\frac{dk^*}{d\theta}$ and $\frac{dx_n}{d\theta}$ via the integrator (6). It holds that

$$\frac{dg^*}{d\theta} = \frac{\partial g^*}{\partial \theta} + \frac{dg^*}{dx_n} \frac{dx_n}{d\theta}. \quad (15)$$

By the dependence of x_{n+1} on g^* and of g^* on x_n , (15) the gradient is backpropagated through time. For an explicit integrator, the gradient $\frac{dk}{d\theta}$ can be computed explicitly, since g_j^* depends on g_i^* with $i < j$. For implicit solvers, the implicit functions theorem [26] is applied. It holds that $g^* = \arg \min_g \eta(k, x_n, \theta)$ with the minimization problem η derived in (9). For the gradients of g^* with respect to x_n respectively θ it holds with the implicit function theorem [26]

$$\frac{dg^*}{dx_n} = \left(\frac{\partial^2 \eta}{\partial g^{*2}} \right)^{-1} \left(\frac{\partial^2 \eta}{\partial x_n \partial g^*} \right). \quad (16)$$

5 Application to symplectic integrators

In summary, we have first derived how to evaluate the implicitly defined RK distributions. Afterward, we have embedded this technique into a recurrent learning scheme and finally, shown how it is trained. Next, we make the method precise for symplectic integrators and Hamiltonian systems.

5.1 Hamiltonian systems and symplectic integrators

An autonomous Hamiltonian system is given by

$$x(t) = \begin{pmatrix} p(t) \\ q(t) \end{pmatrix} \text{ with } \dot{x}(t) = \begin{pmatrix} \dot{p}(t) \\ \dot{q}(t) \end{pmatrix} = \begin{pmatrix} -H_q(p, q) \\ H_p(p, q) \end{pmatrix} \quad (17)$$

and $p, q \in \mathbb{R}^d$. In many applications, q corresponds to the state and p to the velocity. The Hamiltonian H often resembles the total energy and is constant along trajectories. The flow of Hamiltonian systems ψ_t is volume preserving in the sense of $\text{vol}(\psi_t(\Omega)) = \text{vol}(\Omega)$ for each bounded open set Ω . The flow ψ_t describes the solution at time point t for the initial values $x_0 \in \Omega$.

Symplectic integrators are volume preserving for Hamiltonian systems (17) [16]. Thus, $\text{vol}(\Omega) = \text{vol}(\psi_f(\Omega))$ for each bounded Ω . Further, they provide a more accurate approximation of the total energy than standard integrators [16]. When designing the GP, it is critical to respect the Hamiltonian structure (17). Additionally, the symplectic integrator ensures that the volume is indeed preserved.

5.2 Explicit symplectic integrators

A broad class of real world systems can be modeled by separable Hamiltonians $H(p, q) = T(p) + V(q)$. For example, ideal pendulums and the two body problem. Then, for the dynamical system it holds that

$$\dot{p}(t) = -V'(q), \quad \dot{q}(t) = T'(p), \quad (18)$$

with $V : \mathbb{R}^d \rightarrow \mathbb{R}^d$ and $T : \mathbb{R}^d \rightarrow \mathbb{R}^d$. For this class of problems, explicit symplectic integrators can be constructed. In order to ensure Hamiltonian structure, $V'_1(q), \dots, V'_d(q)$ and $T'_1(p), \dots, T'_d(p)$ are modeled with independent sparse GPs. Symplecticity is enforced via discretizing with a symplectic integrator.

Consider for example the explicit symplectic Euler method

$$p_{n+1} = p_n - hV'(q_n), \quad q_{n+1} = q_n + hT'(p_{n+1}). \quad (19)$$

The symplectic Euler method (19) is a partitioned RK method, meaning that different schemes are applied to different dimensions. Here, the explicit Euler method is applied to p_n and the implicit Euler method to q_n . The method (19) is reparametrized as described in Sec. 4.1 by sampling from V' and T' and the scheme can readily be embedded into the inference scheme (cf. Sec. 4.2).

5.3 General symplectic integrators

The general Hamiltonian system (17) requires the application of an implicit symplectic integrator. An example for a symplectic integrator is the midpoint rule applied to (17)

$$x_{n+1} = x_n + hJ^{-1}\nabla H\left(\frac{x_n + x_{n+1}}{2}\right), \quad (20)$$

with $J^{-1} = \begin{pmatrix} 0 & -1 \\ 1 & 0 \end{pmatrix}$.

Again, it is critical to embed the Hamiltonian structure into the dynamics model by modeling H with a sparse GP. Sampling from (20) requires evaluating the gradient ∇H , which is again a GP [32, 45].

6 Experiments

In this section, we validate our method numerically. In particular, we show that we i) achieve higher accuracy than comparable state-of-the-art methods; ii) demonstrate volume-preserving predictions for Hamiltonian systems and the satisfaction of a quadratic geometric constraint; and iii) illustrate that our method can easily deal with different choices of RK integrators.

6.1 Methods

We construct our structure-preserving GP model (SGPD) by tailoring the RK integrator to the underlying problem. We compare to the following state-of-the-art approaches:

Hamiltonian neural network (HNN) [14]: Deep learning approach that is tailored to respect Hamiltonian structure.

Consistent PR-SSM model (Euler) [7]: Standard variational GP model that corresponds to explicit Euler discretizations. Therefore, we refer to it in the following as Euler. In general all common GP state-space models correspond to the Euler discretization. Here, we use a model similar to [7], but in contrast to [7] we compute consistent predictions via decoupled sampling in order to provide the necessary comparability and since the inconsistent sampling scheme in [7] was criticized in later work [24]. The general framework is more flexible and can also cope with lower-dimensional state observations. Here, we consider the special case, where we assume noisy state measurements.

6.2 Learning task and comparison

In the following, we describe the common setup of all experiments. For each Hamiltonian system, we consider one period of a trajectory as training data and all methods are provided with identical training data. For all experiments, we choose the ARD kernel [32]. We apply the training procedure described in Sec. 4.2 on subtrajectories and perform predictions via sampling of trajectories. In order to draw a fair comparison, we choose similar hyperparameters and number of inducing inputs for our SGPD method and the standard Euler discretization. Details are moved to the appendix. In contrast to our method the HNN requires additional derivative information, either analytical or as finite differences. Here, we assume that analytical derivative information is not available and thus compute finite differences.

We consider a twofold goal: accurate predictions in the L^2 sense and invariant preservation. Predictions are performed by unrolling the first training point over multiple periods of the system trajectory. The L^2 -error is computed via averaging 5 independent samples $\hat{X}_i = \frac{1}{5} \sum_{j=1}^5 \hat{X}_i^j$ and computing $\sqrt{\frac{1}{N} \sum_{i=1}^N \|X_i - \hat{X}_i\|^2}$ with ground truth X . Integrators are volume-preserving if and only if they are divergence free, which requires $\det(\psi') = 1$ [16]. Thus, we evaluate $\det(\psi')$ for the rollouts, which is intractable for the Hamiltonian neural networks. We observed that we can achieve similar results by propagating the GP mean in terms of constraint satisfaction and L^2 -error.

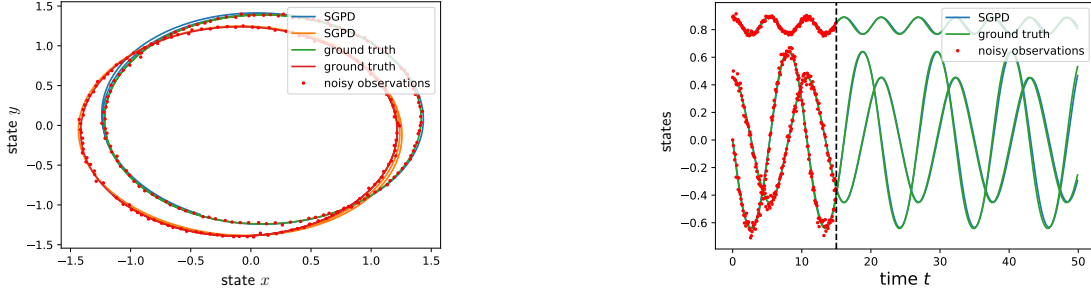


Figure 2: State trajectories for the two-body problem (left) and rigid body dynamics (right). The rigid body dynamics are illustrated as a function over time to show the location of the training data and future behavior of the system. The two-body problem is represented as a phase plot in the two-dimensional space. The first particle q_1 is shown in green and q_2 in red.

Table 1: Shown are the total L^2 -errors in 1a and an analysis of the total energy for the non-separable system 1b.

(a) total L^2 -errors (mean (std) over 5 indep. runs)				(b) Energy for non-separable Hamiltonian		
task	SGPD	Euler	HNN	method	energy err.	std. dev.
(i)	0.421 (0.1)	0.459 (0.12)	4.69 (0.02)	SGPD	$9 \cdot 10^{-4}$	$\cdot 10^{-3}$
(ii)	0.056 (0.01)	0.057 (0.009)	0.12 (0.009)	Euler	10^{-3}	$4 \cdot 10^{-3}$
(iii)	0.033 (0.01)	0.034 (0.021)	0.035 (0.007)	HNN	10^{-3}	$2 \cdot 10^{-3}$
(iv)	0.046 (0.014)	0.073 (0.02)	-			

6.3 Systems and integrators

We consider four different systems here i) ideal pendulum; ii) two-body problem; iii) non-separable Hamiltonian; and iv) rigid body dynamics.

Separable Hamiltonians: the systems i) and ii) are both separable Hamiltonians that are also considered as baseline problems in Greydanus et al. [14]. Due to the similar structure, we can apply the symplectic Euler method (cf. Sec. 5.2) to both problems.

The Hamiltonian of a pendulum is given by $H(p, q) = (1 - 6 \cos(p)) + \frac{p^2}{2}$. Training data is generated from a 10 second ground truth trajectory with discretization $dt = 0.1$ and disturbed with observation noise with variance $\sigma^2 = 0.1$. Predictions are performed on a 40 second interval.

The two body problem models the interaction of two unit-mass particles (p_1, q_1) and (p_2, q_2) , where $p_1, p_2, q_1, q_2 \in \mathbb{R}^2$ and $H(p, q) = \frac{1}{2} + \|p_1\|^2 + \|p_2\|^2 + \frac{1}{\|q_1 - q_2\|^2}$. Noisy training data is generated on an interval of 18.75 seconds, discretization level $dt = 0.15$, and variance $\sigma^2 = 1 \cdot 10^{-3}$. Predictions are performed on an interval of 30 seconds. The orbits of the two bodies q_1 and q_2 are shown in Figure 2 (left).

Non-separable Hamiltonian: As an example for a non-separable Hamiltonian system we consider Eq. (17) with $H(p, q) = \frac{1}{2} [(q^2 + 1)(p^2 + 1)]$ [39]. The implicit

midpoint rule (20) is applied as the numerical integrator (cf. Sec. 5.3). The training trajectory is generated on a 10 seconds interval with discretization $dt = 0.1$ and disturbed with noise with variance $\sigma^2 = 5 \cdot 10^{-4}$. Rollouts are performed on an interval of 40 seconds.

Rigid body dynamics: Consider the rigid body dynamics [16]

$$\begin{pmatrix} \dot{x}_1 \\ \dot{x}_2 \\ \dot{x}_3 \end{pmatrix} = \begin{pmatrix} 0 & \frac{3}{2}x_3 & -x_2 \\ -\frac{3}{2}x_3 & 0 & \frac{x_1}{2} \\ x_2 & -\frac{x_1}{2} & 0 \end{pmatrix} \begin{pmatrix} x_1 \\ x_2 \\ x_3 \end{pmatrix} =: f(x) \quad (21)$$

that describe the angular momentum of a body rotating around an axis. The equations of motion can be derived via a constrained Hamiltonian system. We apply the implicit midpoint method. Since the HNN is designed for non-constrained Hamiltonians it requires pairs of p and q and is, thus, not applicable. Training data is generated on a 15 seconds interval with discretization $dt = 0.1$. Due to different scales, x_1 and x_2 are disturbed with noise with variance $\sigma^2 = 1 \cdot 10^{-3}$, and x_3 is disturbed with noise with variance $\sigma^2 = 1 \cdot 10^{-4}$. Predictions are performed on an interval of 50 seconds (see Figure 2 (right)). The rigid body dynamics preserve the invariant $x_1^2 + x_2^2 + x_3^2 = 1$, which refers to the ellipsoid determined by the axis of the rotating body. We include this property as prior knowledge in our SGPD model via $x^T \hat{f}(x) = 1$ [16]. The dynamics \hat{f} is again trained with independent sparse GPs, where the third

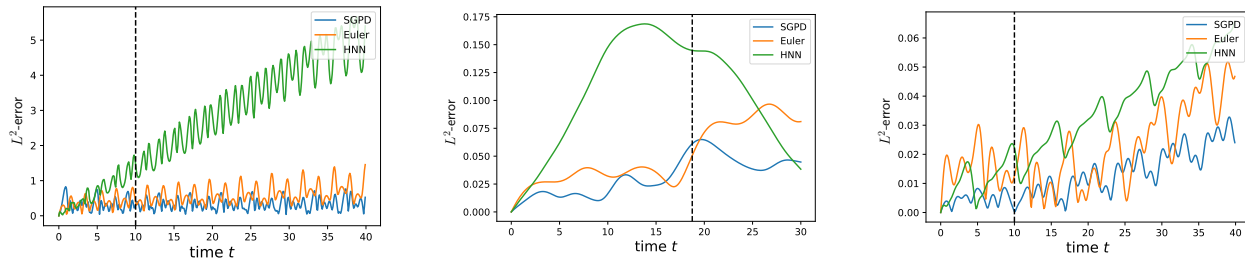


Figure 3: L^2 -errors of averaged state trajectories for all three methods. Shown are the errors for the pendulum (left), the two-body problem (middle), and the non-separable Hamiltonian (right). The training horizon is marked.

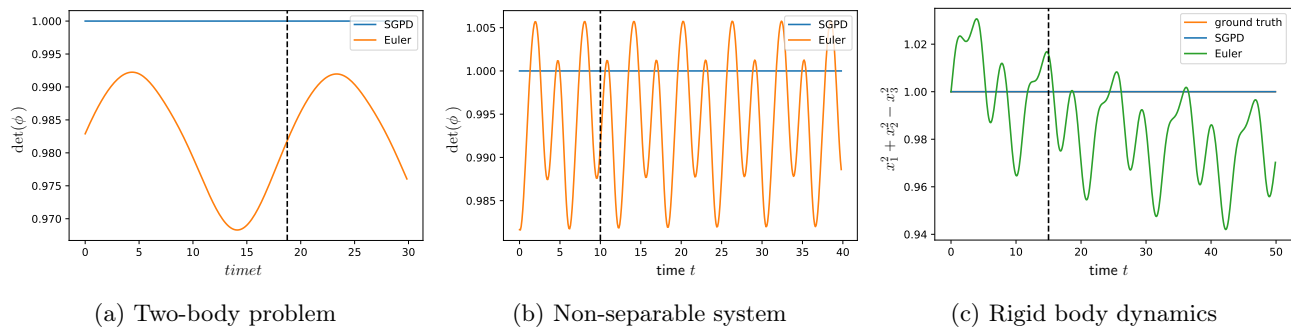


Figure 4: The proposed SGPD (blue) preserves structure: The analytic volume is preserved via SGPD for the Hamiltonian systems in 4a and 4b, while simulations show that the explicit Euler (orange) does not preserve volume. Further, the SGPD rollout preserves the quadratic constraint over time for the rigid body system in 4c, while the standard GP with explicit Euler does not.

dimension is obtained by solving $\hat{f}(x) = 1 - \frac{\hat{f}_1 x_1 + \hat{f}_2 x_2}{x_3}$.

6.4 Results

In summary, our method shows the smallest L^2 -error (see Table 1a). The evolution of L^2 -errors is illustrated in Figure 3 for the pendulum (left), two-body problem (middle), and non-separable system (right) and show how the other methods accumulate errors.

For systems (i),(ii), and (iii), we demonstrate volume preservation. Figure 4 shows that volume is preserved for the symplectic integrator-based SGPD in contrast to the standard explicit Euler method. For the rigid body dynamics, we consider the invariant $x_1^2 + x_2^2 + x_3^2 = 1$. Figure 4c demonstrates that the implicit midpoint is able to approximately preserve the invariant along the whole rollout. In contrast, the explicit Euler fails even though it provides comparable accuracy in terms of L^2 -error.

The midpoint method-based SGPD furthermore shows accurate approximation of the constant total energy for the systems (iii) and (iv). The total energy corresponds to the Hamiltonian H for system (iii). We average the approximated energy along 5 independent trajectories $H_n = \sum_{i=1}^5 \frac{H_n^i}{5}$ and compute the average total en-

ergy $\hat{H} = \frac{1}{n} \sum_n H_n$. Afterwards we evaluate the error $\|H - \hat{H}\|$ and the standard deviation $\sqrt{\sum_n \frac{|H_n - H|^2}{n-1}}$ (see Table 1b). Our SGPD method yields the best approximation to the energy. Both methods outperform the explicit Euler method. For the rigid body dynamics, our method yields extremely accurate approximation of the total energy. Details are moved to the Appendix. An empirical evaluation of higher-order methods is moved to the Appendix.

7 Conclusion and future work

In this paper we combine numerical integrators with GP regression. Thus, resulting in an inference scheme that preserves physical properties and yields high accuracy. On a technical level, we derive a method that samples from implicitly defined distributions. By the means of empirical comparison, we show the advantages over Euler-based state-of-the-art methods that are not able to preserve physical structure. Of course, our method critically relies on physical prior knowledge. However, this insight is often available. An important extension that we want to address in the future are state observations, control input, and continuous-time dynamics.

Bibliography

- [1] Abdulle, A. and Garegnani, G. (2020). Random time step probabilistic methods for uncertainty quantification in chaotic and geometric numerical integration. *Statistics and Computing*, 30(4):907–932.
- [2] Bai, S., Kolter, J. Z., and Koltun, V. (2019). Deep equilibrium models. In *Advances in Neural Information Processing Systems 32*, pages 690–701.
- [3] Brüdigam, J., Schuck, M., Capone, A., Sosnowski, S., and Hirche, S. (2021). Structure-preserving learning using Gaussian processes and variational integrators. *arXiv:2112.05451*.
- [4] Buisson-Fenet, M., Solowjow, F., and Trimpe, S. (2020). Actively learning Gaussian process dynamics. In *Proceedings of the 2nd Conference on Learning for Dynamics and Control*. PMLR.
- [5] Chen, Z., Zhang, J., Arjovsky, M., and Bottou, L. (2020). Symplectic recurrent neural networks. In *8th International Conference on Learning Representations, ICLR 2020*.
- [6] Deisenroth, M. P. and Rasmussen, C. E. (2011). Pilco: A model-based and data-efficient approach to policy search. In *In Proceedings of the International Conference on Machine Learning (ICML)*.
- [7] Doerr, A., Daniel, C., Schiegg, M., Nguyen-Tuong, D., Schaal, S., Toussaint, M., and Trimpe, S. (2018). Probabilistic recurrent state-space models. In *Proceedings of the International Conference on Machine Learning (ICML)*.
- [8] Eleftheriadis, S., Nicholson, T. F., Deisenroth, M. P., and Hensman, J. (2017). Identification of Gaussian process state space models. In *Proceedings of the 31st International Conference on Neural Information Processing Systems, NIPS’17*, page 5315–5325.
- [9] Föll, R., Haasdonk, B., Hanselmann, M., and Ulmer, H. (2019). Deep recurrent Gaussian process with variational sparse spectrum approximation. *arxiv:1909.13743*.
- [10] Frigola, R., Chen, Y., and Rasmussen, C. (2014). Variational Gaussian process state-space models. *Advances in Neural Information Processing Systems 27 (NIPS 2014)*, pages 3680–3688.
- [11] Geist, A. and Trimpe, S. (2020). Learning constrained dynamics with Gauss’ principle adhering Gaussian processes. In *Learning for Dynamics and Control*, pages 225–234. PMLR.
- [12] Girvin, S. M. and Yang, K. (1994). *Modern condensed matter physics*. Cambridge University Press.
- [13] Gould, S., Hartley, R., and Campbell, D. (2019). Deep declarative networks: A new hope. *arXiv:1909.04866*.
- [14] Greydanus, S., Dzamba, M., and Yosinski, J. (2019). Hamiltonian neural networks. In *Advances in Neural Information Processing Systems 32*, pages 15379–15389.
- [15] Haber, E. and Ruthotto, L. (2017). Stable architectures for deep neural networks. *Inverse Problems*, 34.
- [16] Hairer, E., Lubich, C., and Wanner, G. (2006). *Geometric numerical integration: structure-preserving algorithms for ordinary differential equations*. Springer.
- [17] Hairer, E., Nørsett, S., and Wanner, G. (1987). *Solving Ordinary Differential Equations I – Nonstiff Problems*. Springer.
- [18] Hairer, E. and Wanner, G. (1996). *Solving Ordinary Differential Equations II – Stiff and Differential-Algebraic Problems*. Springer.
- [19] Hegde, P., Çağatay Yıldız, Lähdesmäki, H., Kaski, S., and Heinonen, M. (2021). Bayesian inference of ODEs with Gaussian processes. *arXiv:2106.10905*.
- [20] Heinonen, M. and d’Alché Buc, F. (2014). Learning nonparametric differential equations with operator-valued kernels and gradient matching. *arXiv:1411.5172*.
- [21] Heinonen, M., Yildiz, C., Mannerström, H., Intosalmi, J., and Lähdesmäki, H. (2018). Learning unknown ODE models with Gaussian processes. In *Proceedings of the 35th International Conference on Machine Learning*.
- [22] Hensman, J., Fusi, N., and Lawrence, N. (2013). Gaussian processes for big data. *Uncertainty in Artificial Intelligence - Proceedings of the 29th Conference, UAI 2013*.
- [23] Howarth, R. J. (1979). Mining geostatistics. London & New York (academic press), 1978. *Mineralogical Magazine*, 43:1–4.
- [24] Ialongo, A. D., Van Der Wilk, M., Hensman, J., and Rasmussen, C. E. (2019). Overcoming mean-field approximations in recurrent Gaussian process models. In *Proceedings of the 36th International Conference on Machine Learning (ICML)*.
- [25] Jin, P., Zhang, Z., Zhu, A., Tang, Y., and Karniadakis, G. E. (2020). Sympnets: Intrinsic structure-preserving symplectic networks for identifying Hamiltonian systems. *arXiv:2001.03750*.
- [26] Krantz, S. and Parks, H. (2013). *The implicit function theorem. History, theory, and applications. Reprint of the 2003 hardback edition*.
- [27] Ljung, L. (1999). System identification. *Wiley encyclopedia of electrical and electronics engineering*, pages 1–19.

- [28] Look, A., Doneva, S., Kandemir, M., Gemulla, R., and Peters, J. (2020). Differentiable implicit layers. In *Workshop on machine learning for engineering modeling, simulation and design at NeurIPS 2020*.
- [29] Nguyen-Tuong, D. and Peters, J. (2011). Model learning for robot control: A survey. *Cognitive processing*, 12:319–40.
- [30] Pan, Y., Imani, E., Farahmand, A.-m., and White, M. (2020). An implicit function learning approach for parametric modal regression. In *Advances in Neural Information Processing Systems*, volume 33, pages 11442–11452.
- [31] Rahimi, A. and Recht, B. (2008). Random features for large-scale kernel machines. In *Advances in Neural Information Processing Systems*, volume 20.
- [32] Rasmussen, C. E. and Williams, C. K. I. (2005). *Gaussian Processes for Machine Learning (Adaptive Computation and Machine Learning)*. The MIT Press.
- [33] Rath, K., Albert, C. G., Bischl, B., and von Toussaint, U. (2021). Symplectic Gaussian process regression of maps in Hamiltonian systems. *Chaos*, 31 5:053121.
- [34] Saemundsson, S., Terenin, A., Hofmann, K., and Deisenroth, M. P. (2020). Variational integrator networks for physically structured embeddings. In *Proceedings of the 23rd International Conference on Artificial Intelligence and Statistics (AISTATS)*, volume 108.
- [35] Sakurai, J. J. (1994). *Modern quantum mechanics; rev. ed.* Addison-Wesley.
- [36] Salmon, R. (2003). Hamiltonian fluid mechanics. *Annual Review of Fluid Mechanics*, 20:225–256.
- [37] Schön, T. B., Wills, A., and Ninness, B. (2011). System identification of nonlinear state-space models. *Automatica*, 47(1):39–49.
- [38] Svensson, A., Solin, A., Särkkä, S., and Schön, T. B. (2016). Computationally efficient Bayesian learning of Gaussian process state space models. *arxiv:1506.02267*.
- [39] Tao, M. (2016). Explicit symplectic approximation of nonseparable Hamiltonians: Algorithm and long time performance. *Physical Review E*, 94(4).
- [40] Titsias, M. (2009). Variational learning of inducing variables in sparse Gaussian processes. *Journal of Machine Learning Research - Proceedings Track*, pages 567–574.
- [41] Turner, R., Deisenroth, M., and Rasmussen, C. (2010). State-space inference and learning with Gaussian processes. *Journal of Machine Learning Research - Proceedings Track*, 9:868–875.
- [42] Wang, J., Fleet, D., and Hertzmann, A. (2008). Gaussian process dynamical models for human motion. *IEEE transactions on pattern analysis and machine intelligence*, 30:283–98.
- [43] Wenk, P., Gotovos, A., Bauer, S., Gorbach, N., Krause, A., and Buhmann, J. M. (2019). Fast Gaussian process based gradient matching for parameter identification in systems of nonlinear ODEs. In *Proceedings of the 22nd International Conference on Artificial Intelligence and Statistics (AISTATS)*, pages 1351–1360.
- [44] Wilson, J. T., Borovitskiy, V., Terenin, A., Mostowsky, P., and Deisenroth, M. P. (2020). Efficiently sampling functions from Gaussian process posteriors. *arXiv:2002.09309*.
- [45] Yang, A., Li, C., Rana, S., Gupta, S., and Venkatesh, S. (2018). *Sparse Approximation for Gaussian Process with Derivative Observations: 31st Australasian Joint Conference, Wellington, New Zealand, December 11-14, 2018, Proceedings*, pages 507–518.
- [46] Zhong, Y. D., Dey, B., and Chakraborty, A. (2020). Symplectic ODE-net: Learning Hamiltonian dynamics with control. In *8th International Conference on Learning Representations, ICLR 2020*.

Structure-preserving Gaussian Process Dynamics: Supplementary Materials

arXiv:2102.01606v3 [cs.LG] 9 Jan 2022

1 Additional experiments

We provide additional plots in order to illustrate the results from Section 6. Furthermore we add uncertainty information to the SGPD predictions for all experiments in Section 6. We extend the results for the rigid body dynamics experiment by demonstrating the evolution of energy. In order to illustrate properties of higher-order integrators we provide additional experiments.

Figure 1 shows additional plots for the results in Section 6. Shown are SGPD rollouts for the pendulum problem (left), the non-separable Hamiltonian system (middle), and the determinant of the pendulum problem (right).

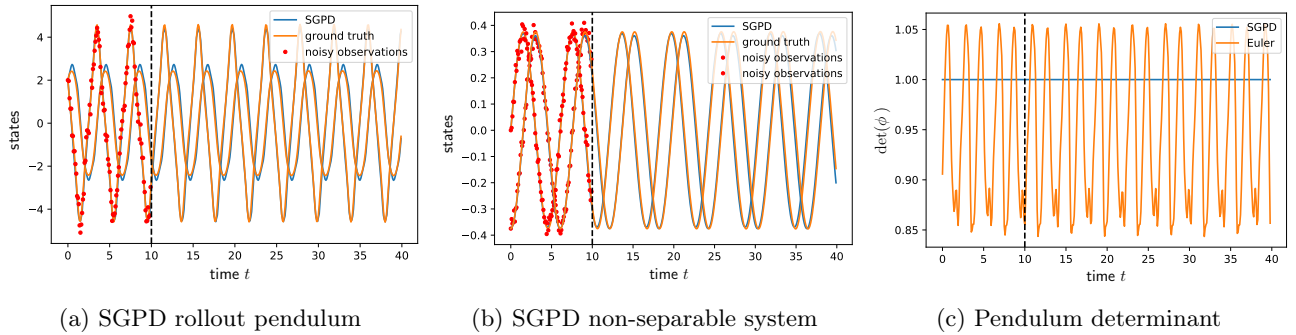


Figure 1: Additional plots for the experiments in Section 6. Shown are state trajectories for the pendulum (left) and non-separable Hamiltonian system (middle). Both systems are illustrated as a function over time to show the location of the training data and future behavior of the system. The determinant of the pendulum problem is depicted (right) indicating that the explicit Euler method is not preserving structure.

1.1 Uncertainty

We add uncertainty information to the SGPD predictions by sampling 5 trajectories $X_n^i, i = 1, \dots, 5$ from the trained models (cf. Section 6). Mean μ_n and standard deviation σ_n are approximated via

$$\begin{aligned} \mu_n &= \frac{1}{5} \sum_{i=1}^5 X_n^i \\ \sigma_n &= \sqrt{\frac{1}{4} \sum_{i=1}^5 (X_n^i - \mu_n)^2}. \end{aligned} \tag{1}$$

Plots for all experiments are shown in Figure 2.

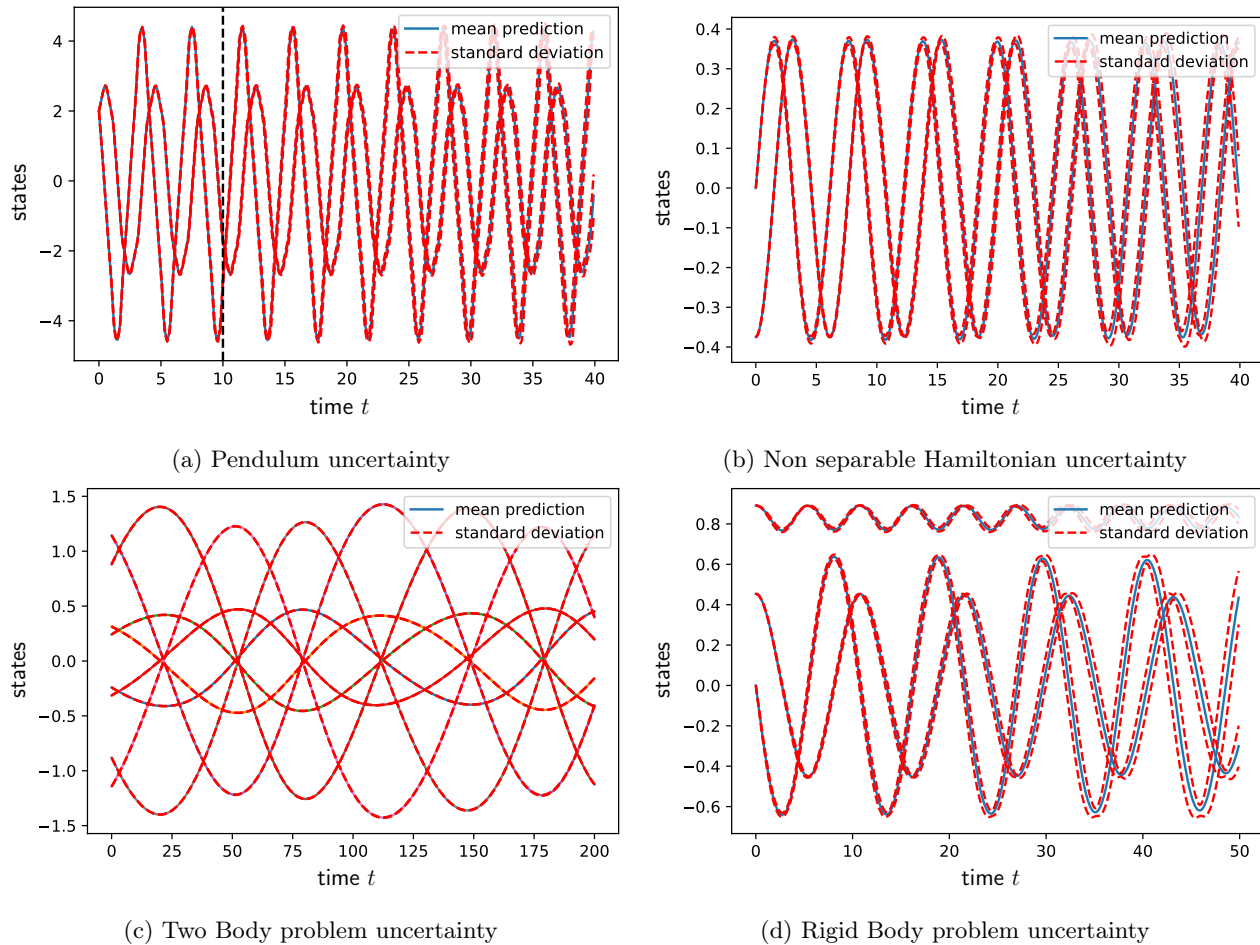


Figure 2: Uncertainty information for the SGPD predictions from Section 6. Shown are mean (blue) and standard deviation (red) of 5 rollouts for the pendulum problem 2a, the non-separable Hamiltonian 2b, the two-body problem 2c and the rigid body dynamics 2d.

1.2 Rigid body dynamics

We demonstrate that our SGPD method produces an accurate approximation to the total energy for the rigid body dynamics (cf. Section 6) in contrast to the standard explicit Euler dynamics. The constant ground truth energy E is given $E = \frac{x_1^2}{2} + x_2^2 + \frac{3x_3^2}{2}$. We evaluate this equation for the SGPD and explicit Euler trajectories by averaging over the 5 sampled trajectories $E_n = \sum_{i=1}^5 E_n^i$. We compute the approximated average energy $\hat{E} = \sum_n \frac{E_n}{n}$ and evaluate the error $\|E - \hat{E}\|$ and the standard deviation $\sqrt{\sum_n \frac{|E_n - E|^2}{n-1}}$ along the trajectory. The results are shown in Figure 3.

1.3 Higher-order integrators

We demonstrate further benefits of our SGPD model learning scheme (cf. Section 4). In detail, we apply our method to a higher-order integrator. This yields a model that is less sensitive to varying step sizes for training and predictions than a model trained with the standard explicit Euler approach.

The number and choice of the internal stages determine the approximation order of a Runge-Kutta method ψ_f [2] (cf. Section 3). Let $x(t)$ be the ground truth solution of the continuous time dynamical system $\dot{x}(t) = f(x(t))$ and let $e = x(t) + h\psi_f(x(t)) - x(t+h)$ be the local error. For a Runge-Kutta method with order p it holds that

$$\|e\|_\infty \leq Ch^{p+1}. \quad (2)$$

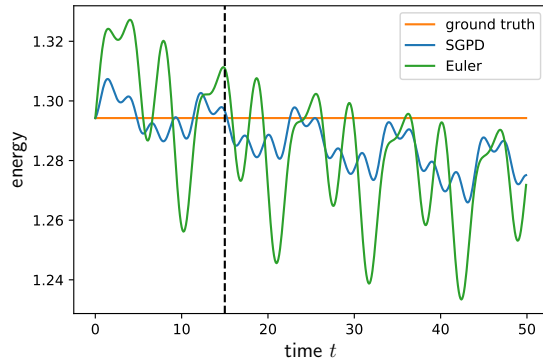


Figure 3: Evaluation of the energy for the rigid body dynamics. Shown are the evolution of the energy (left) and the results for the analysis of the total energy (right). The SGPD preserves the energy more accurately than the explicit Euler method.

Intuitively, the higher the order, the smaller the error and the better the numerical approximation $x(n)$ (cf. Section 3). For the explicit Euler it holds that $p = 1$. When choosing a higher-order Runge-Kutta integrator for dynamics model learning (cf. Section 3) the learned dynamics \hat{f} provide a more accurate approximation to the ground truth dynamics f than the standard explicit Euler dynamics model. Thus, predictions can be made with varying step size. We demonstrate the flexibility empirically by comparing the standard explicit Euler method to the second order Heun method

$$\begin{aligned}
 k_1 &= f(x_n), k_2 = f(x_n + hk_1) \\
 x_{n+1} &= x_n + \frac{h}{2}(k_1 + k_2).
 \end{aligned} \tag{3}$$

Both models are trained with step size $h = 10^{-1}$ on a horizon of 10 seconds. We demonstrate that our Heun-based SGPD method is able to perform predictions with varying step sizes in contrast to the explicit Euler method. To this end we compute predictions with half of the training step size $h = 5 \cdot 10^{-3}$. The SGPD method provides an accurate trajectory (Fig. 4f), while the explicit Euler method fails (Fig. 4c). Further, we demonstrate that the SGPD dynamics \hat{f} are close to the ground truth dynamics f by applying an adaptive step size solver to the predictions. This type of solver controls the numerical error e in Eq. (2) and adapts the step size accordingly. Again, the SGPD model provides accurate predictions (Fig. 4e), while the explicit Euler model fails (Fig. 4b). Intuitively, the SGPD dynamics provide good results when being treated as continuous time dynamical system. The explicit Euler dynamics on the other hand correspond to a discrete-time model that is adapted to the training step size.

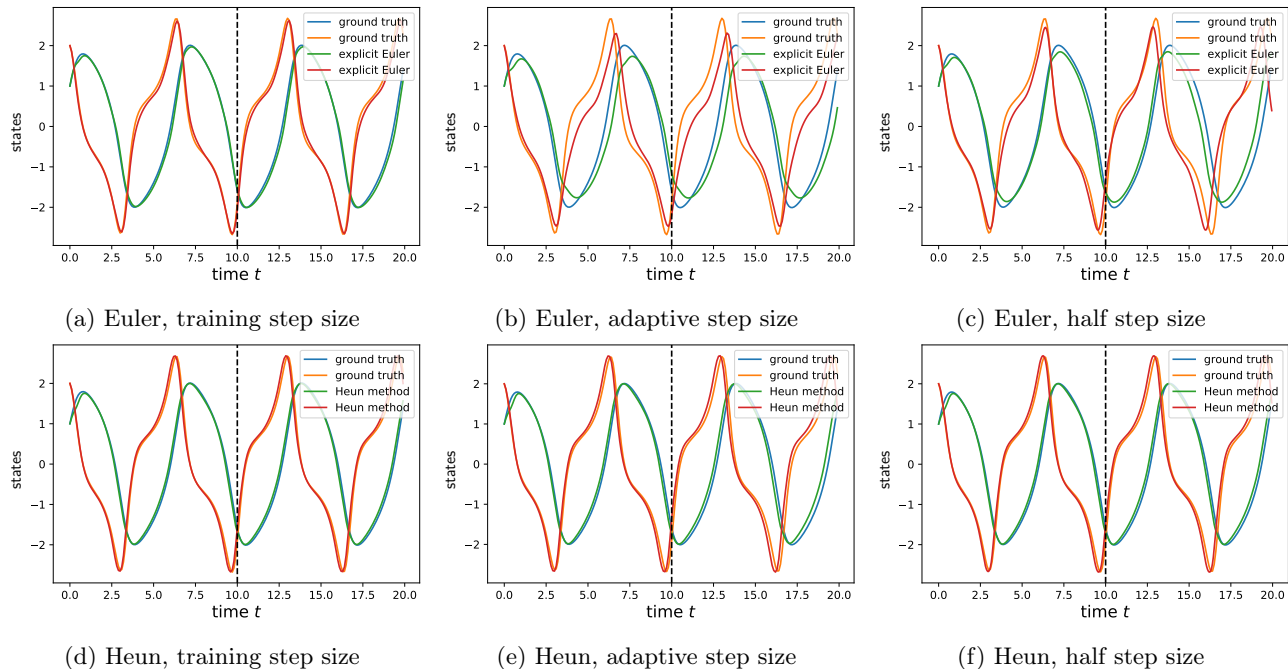


Figure 4: The Heun-based SGPD method is able to make accurate predictions with varying step sizes, while the explicit Euler method is adapted to the training step size $h = 10^{-1}$. Shown are the results for the explicit Euler method (upper row) and the Heun-based SGPD method (lower row) for predictions with step size $h = 10^{-1}$ (left), adaptive step size (middle) and step size $h = 5 \cdot 10^{-3}$ (right).

2 Experimental setup

We give a more detailed explanation of our experimental setup. The experiments were performed on a desktop CPU. The main libraries used for computation are Paszke et al. [6] and Harris et al. [3]. For the plots and presentation Hunter [5] was used.

Initialization: We choose the ARD kernel $k(x, x') = \sigma_f^2 \exp\left(-\sum_{i=1}^d \frac{(x_i - x'_i)^2}{2l_i^2}\right)$. Hyperparameters include kernel parameters σ_f, l , variational sparse GP parameters $\mu_{\xi, i}, \Sigma_{\xi}$ (cf. Section 3), and the positions of the inducing inputs ξ . The initialization of the GP hyperparameters is shown in Table 1 for the SGPD method and in Table 2 for the explicit Euler method. The number of inducing inputs per GP is denoted N_{ξ} . The total number of inducing inputs is always the same or higher for the explicit Euler model compared to the SGPD model. For all experiments, except the two-body problem, all independent sparse GPs are initialized with the same hyperparameters. For the two-body problem the GP lengthscales are different for each dimension. Table 3 contains the SGPD lengthscales and Table 4 the explicit Euler lengthscales for the two-body problem.

Table 1: Hyperparameters SGPD

method	σ_f^2	l_i^2	$\mu_{\xi, i}$	Σ_{ξ}	N_{ξ}
pendulum	0.01	$\sqrt{2}$	$\mathcal{N}(0, 0.05^2)$	$10^{-8} \cdot \mathbf{I}$	9
two-body problem	10^{-4}	Table 3	$\mathcal{N}(0, 0.05^2)$	$10^{-8} \cdot \mathbf{I}$	20
non-separable system	10^{-4}	2	$\mathcal{N}(0, 0.05^2)$	$10^{-7} \cdot \mathbf{I}$	16
rigid body dynamics	10^{-3}	1	$\mathcal{N}(0, 0.05^2)$	$10^{-6} \cdot \mathbf{I}$	9

Inducing inputs: For the pendulum problem with SGPD ξ_p lie on a uniform grid on the interval $[-5, 5]$ and ξ_q lie on a uniform grid on the interval $[-3, 3]$. For the explicit Euler method ξ lie on the corresponding two-dimensional interval with $-5 \leq p \leq 5$ and $-3 \leq q \leq 3$.

Table 2: Hyperparameters explicit Euler

method	σ_f^2	l_i^2	$\mu_{\xi,i}$	Σ_ξ	N_ξ
pendulum	0.01	$\sqrt{2}$	$\mathcal{N}(0, 0.05^2)$	$10^{-8} \cdot \mathbf{I}$	9
two-body problem	10^{-4}	Table 4	$\mathcal{N}(0, 0.05^2)$	$10^{-8} \cdot \mathbf{I}$	20
non-separable system	10^{-4}	2	$\mathcal{N}(0, 0.05^2)$	$10^{-7} \cdot \mathbf{I}$	9
rigid body	10^{-5}	1	$\mathcal{N}(0, 0.05^2)$	$10^{-8} \cdot \mathbf{I}$	11

Table 3: Lengthscale SGPD two-body problem

dimension	l_1^2	l_2^2	l_3^2	l_4^2
p_1	8.52	4.97	8.52	4.97
p_2	9.0	4.62	9.0	4.62
p_3	8.52	4.97	8.52	4.97
p_4	9.0	4.62	9.0	4.62
q_1	169	841	169	841
q_2	256	324	129	324
q_3	169	841	169	841
q_4	256	324	129	324

For the two-body problem with SGPD it holds that $\xi_{p,1:4} \sim \mathcal{N}(-1.1, 2.2^2)$, $\xi_{q,1:4} \sim \mathcal{N}(-0.7, 1.4^2)$. For the two-body problem with explicit Euler method the same configuration holds true on the corresponding 8-dimensional interval.

For the non-separable Hamiltonian problem the inducing inputs are initialized on the uniform grid on the two-dimensional interval $[-0.5, 0.5]$.

For the rigid body dynamics with SGPD the inducing inputs are initialized on the two-dimensional interval with $x \in [-0.5, 0.5]$ and $y \in [-0.7, 0.7]$. For the explicit Euler method the inducing inputs are initialized via $x \in \mathcal{N}(-0.5, 1)$, $y \in \mathcal{N}(-0.7, 1.7^2)$, $z \in \mathcal{N}(0.7, 0.2^2)$.

Dataset: For all experiments recurrent training (cf. Section 4) is performed on subtrajectories of the training trajectory. The trajectory is split into a dataset of all possible subtrajectories by choosing initial values via a sliding window with step size 1. Training is performed via epochs over the dataset of all subtrajectories. Shuffling and batching of the dataset is performed via Pytorch dataloader [6]. Adam optimizer is applied for training. The training configuration is shown in Table 5 for all systems. Our SGPD method and the standard explicit Euler method are trained with the same configurations.

Initial value: We observe noisy initial values \hat{x}_0 (cf. Section 1). During training we choose $x_0 = \hat{x}_0$.

Tolerance of the implicit solver: The implicit integrators require solving a nonlinear system of equations.

Table 4: Lengthscale SGPD two-body problem

dimension	l_1^2	l_2^2	l_3^2	l_4^2	l_5^2	l_6^2	l_7^2	l_8^2
p_1	8.52	4.97	8.52	4.97	8.52	4.97	8.52	4.97
p_2	9.0	4.62	9.0	4.62	9.0	4.62	9.0	4.62
p_3	8.52	4.97	8.52	4.97	8.52	4.97	8.52	4.97
p_4	9.0	4.62	9.0	4.62	9.0	4.62	9.0	4.62
q_1	169	841	169	841	169	841	169	841
q_2	256	324	129	324	256	324	129	324
q_3	169	841	169	841	169	841	169	841
q_4	256	324	129	324	256	324	129	324

Table 5: Training configuration

system	batch size	subtrajectory length
pendulum	1	10
two-body problem	5	50
non-separable system	1	10
rigid body	1	20

We choose the Levenberg-Marquardt solver implemented in Virtanen et al. [7] with the default configuration.

Loss function: The loss is computed via the ELBO (cf. Section 4). We balance the influence of the KL-divergence with respect to the total loss with factors a and b . The loss \mathcal{L} is then computed $\mathcal{L} = a \log p(\hat{x}_n|x_n) - b \text{KL}(p(z)||q(z))$. The chosen factors are documented in Table 6.

Table 6: ELBO factors

system	a	b
pendulum	4	10^{-6}
two-body problem	20	10^{-6}
non-separable system	1	10^{-6}
rigid body	20	1

Decoupled sampling: We sample from GPs via decoupled sampling

$$\begin{aligned}
 f(x^*|z, \xi) &= \underbrace{f(x^*)}_{\text{prior}} + \underbrace{k(x^*, \xi)k(\xi, \xi)^{-1}(z - f_z)}_{\text{update}} \\
 &\approx \sum_{i=1}^S w_i \phi_i(x^*) + \sum_{j=1}^M v_j k(x^*, \xi_j)(z - f_z).
 \end{aligned} \tag{4}$$

For the ARD kernel $k(x, x') = \sigma_f^2 \exp\left(-\sum_{i=1}^d \frac{(x_i - x'_i)^2}{2l_i^2}\right)$ it holds that $\phi_i(x) = \sqrt{\frac{\sigma_f^2}{S}}(\cos x^T \omega_i, \sin x^T \omega_i)$. The parameters ω_i are sampled proportional to the spectral density of the kernel $\omega_i \sim \mathcal{N}(0, \Lambda^{-1})$, where $\Lambda = \text{diag}(l_1^2, l_2^2, \dots, l_d^2)$. For the ARD kernel this results in $2S$ feature maps $\phi(x) \in \mathbb{R}^{2S}$. Weights $w \in \mathbb{R}^{2S}$ are sampled from a standard normal $w_i \sim \mathcal{N}(0, 1)$ [4]. We choose $S = 10000$ for our experiments.

Model selection: Let $\hat{X}_i = \frac{1}{5} \sum_{j=1}^5 \hat{X}_i^j$, $i = 1 \dots n$ be the average of 5 rollouts and $\hat{x}_{1:n}$ the noisy observations. In order to obtain the best model we compute $e = \sum_{i=1}^n \|\hat{X}_i - \hat{x}_i\|^2$ at the beginning of every epoch. After training we choose the model with the smallest error e . In case the learning rate is adapted during training we apply the model selection criterion to models corresponding to the smallest learning rate.

Learning rates and model selection: The pendulum problem is trained for 149 epochs with an initial learning rate of 10^{-2} for the SGPD and the explicit Euler method. Model selection is performed over all epochs. The two-body problem is trained for 149 epochs with an initial learning rate 10^{-2} . After 100 epochs the learning rate is lowered to 10^{-3} for the SGPD and the explicit Euler method. Model selection is performed on the final 45 epochs for the SGPD and the explicit Euler method.

For the non-separable Hamiltonian system our SGPD method is trained for 10 epochs with an initial learning rate of 10^{-4} . After 2 epochs the learning rate is set 10^{-2} , after 5 epochs it is set 10^{-5} . Model selection is performed on the final 5 epochs.

The nonseparable Hamiltonian system with explicit Euler method is trained for 49 epochs with learning rate of 10^{-3} . Model selection is performed over all epochs.

The rigid-body dynamics with SGPD is trained for 11 epochs with an initial learning rate of 10^{-2} . Each two

epochs the learning rate is scaled with a factor 10^{-1} up to the final learning rate 10^{-5} . Model selection is performed over the final 4 epochs.

The rigid body dynamics with explicit Euler method is trained for 20 epochs with an initial learning rate of 10^{-2} . After 10 epochs the learning rate is set 10^{-3} , after 10 epochs it is set 10^{-4} . Model selection is performed over all epochs.

Training data: Training data are generated from ground truth and disturbed with noise as described in Section 6. Initial values are chosen $(2, 2)$ for the pendulum problem, $(0, -1.5/4)$ for the non-separable Hamiltonian system and $(\cos(1.1), 0, \sin(1.1))$ for the rigid body dynamics and $(1.144, 0.880, -0.241, 0.313, -1.144, -0.880, 0.241, -0.313)$ for the two-body problem. For the two-body problem we generate the data via the generator provided in Greydanus et al. [1] with `orbit`, `settings = get_orbit(state, t_points=201, t_span = [0, 30], rtol = 1e-10)` and numpy random seed 30.

Bibliography

- [1] Greydanus, S., Dzamba, M., and Yosinski, J. (2019). Hamiltonian neural networks. In *Advances in Neural Information Processing Systems 32*, pages 15379–15389.
- [2] Hairer, E., Nørsett, S., and Wanner, G. (1987). *Solving Ordinary Differential Equations I – Nonstiff Problems*. Springer.
- [3] Harris, C. R., Millman, K. J., van der Walt, S. J., Gommers, R., Virtanen, P., Cournapeau, D., Wieser, E., Taylor, J., Berg, S., Smith, N. J., Kern, R., Picus, M., Hoyer, S., van Kerkwijk, M. H., Brett, M., Haldane, A., del R'io, J. F., Wiebe, M., Peterson, P., G'erard-Marchant, P., Sheppard, K., Reddy, T., Weckesser, W., Abbasi, H., Gohlke, C., and Oliphant, T. E. (2020). Array programming with NumPy. *Nature*, 585(7825):357–362.
- [4] Hegde, P., Çağatay Yıldız, Lähdesmäki, H., Kaski, S., and Heinonen, M. (2021). Bayesian inference of ODEs with Gaussian processes. *arXiv:2106.10905*.
- [5] Hunter, J. D. (2007). Matplotlib: A 2D graphics environment. *Computing in Science & Engineering*, 9(3):90–95.
- [6] Paszke, A., Gross, S., Massa, F., Lerer, A., Bradbury, J., Chanan, G., Killeen, T., Lin, Z., Gimelshein, N., Antiga, L., Desmaison, A., Kopf, A., Yang, E., DeVito, Z., Raison, M., Tejani, A., Chilamkurthy, S., Steiner, B., Fang, L., Bai, J., and Chintala, S. (2019). Pytorch: An imperative style, high-performance deep learning library. In *Advances in Neural Information Processing Systems 32*, pages 8024–8035.
- [7] Virtanen, P., Gommers, R., Oliphant, T. E., Haberland, M., Reddy, T., Cournapeau, D., Burovski, E., Peterson, P., Weckesser, W., Bright, J., van der Walt, S. J., Brett, M., Wilson, J., Millman, K. J., Mayorov, N., Nelson, A. R. J., Jones, E., Kern, R., Larson, E., Carey, C. J., Polat, İ., Feng, Y., Moore, E. W., VanderPlas, J., Laxalde, D., Perktold, J., Cimrman, R., Henriksen, I., Quintero, E. A., Harris, C. R., Archibald, A. M., Ribeiro, A. H., Pedregosa, F., van Mulbregt, P., and SciPy 1.0 Contributors (2020). SciPy 1.0: Fundamental Algorithms for Scientific Computing in Python. *Nature Methods*, 17:261–272.